Theoretical and computational studies of the Weibel instability in several beam–plasma interaction configurations

Conor Davidson [1,2,†], **Zheng-Ming Sheng**[1,2,3,4], **Thomas Wilson**[1,2] **and Paul McKenna**[1,2]

[1]Department of Physics, SUPA, University of Strathclyde, Glasgow G4 0NG, UK

[2]Cockcroft Institute, Sci-Tech Daresbury, Cheshire WA4 4AD, UK

[3]Key Laboratory for Laser Plasmas (MoE) and School of Physics and Astronomy, Shanghai Jiao Tong University, Shanghai 200240, PR China

[4]Tsung-Dao Lee Institute, Shanghai 200240, PR China

The Weibel instability is investigated theoretically and numerically under three scenarios: counterstreaming electron beams in background plasma, an electron–positron beam and an electron–proton beam in background plasma. These models occur widely in laboratory and astrophysical environments. The Weibel instability growth rates are determined numerically from the corresponding cold-fluid dispersion relations, which are confirmed with two-dimensional particle-in-cell simulations. The maximum growth rates for the counterstreaming beams in background plasma are an order of magnitude smaller than the maximum growth rates for the beams cases in the same range of density ratios and beam energies. The maximum growth rate for the electron–positron beam case is shown to be at most a factor $\sqrt{2}$ greater than the electron–proton beam case with similar dispersion behaviours. A non-monotonic relation is found between the maximum Weibel instability growth rates and the electron–positron beam energy, suggesting that increasing beam energies does not entail an increase in the Weibel instability growth rate.

Key words: plasma instabilities, plasma simulation, plasma flows

1. Introduction

The mechanisms by which high-energy cosmic rays are accelerated is an unresolved issue which attracts considerable attention. Fermi proposed that the interaction between particles and magnetic fields in the cosmic environment was responsible for the inverse power law spectra of the cosmic radiation (Fermi 1949): this is known as Fermi acceleration. Fermi acceleration is expected in collisionless shocks found in extreme astrophysical environments (Sagdeev 1966; Tidman 1969) which grow from Weibel instabilities (Weibel 1959). In the astrophysical context, the only way to probe these acceleration mechanisms is from telescopic observation of their radiation spectra. With the

† Email address for correspondence: c.davidson@strath.ac.uk

development of high-power lasers (Maine *et al.* 1988) and advanced diagnostic techniques, a new field of laboratory astrophysics has been opened up (Remington *et al.* 1999). This allows for aspects of these astrophysical environments to be mimicked in a laboratory setting where the plasmas can be probed directly with diagnostics and compared with numerical simulations (Dawson 1983). For example, the interaction between intense relativistic laser light with solid targets can accelerate ions to high energies under various mechanisms (Passoni, Bertagna & Zani 2010), including shock formation (He *et al.* 2007). Furthermore, direct observation of turbulent magnetic fields in hot dense laser target interactions has been reported (Mondal *et al.* 2012). The dynamics of plasma beams have been explored experimentally and with simulations (Hsu *et al.* 2015; Liu *et al.* 2017). The interaction between colliding plasma beams shows magnetic compression and experimental evidence of proton acceleration (Higginson *et al.* 2019).

Furthermore, the collision of relativistic beams with plasma mimicking the background interstellar medium near young stellar objects and Herbig–Haro objects has been investigated (Gregory *et al.* 2008; Valenzuela *et al.* 2015). Lepton beams into background electron–proton plasmas are a promising source of high-energy cosmic rays via Weibel-induced moving magnetic islands (Cui *et al.* 2015) and can show preferential positron acceleration (Dieckmann *et al.* 2020). The interaction of relativistic plasmas, electron–proton or leptonic, with background plasma are of great importance in the study of these extreme astrophysical environments. Understanding the theoretical dispersion relations of the Weibel instability in these plasmas is crucial.

There has been extensive work in the field of plasma instabilities. Counterstreaming electron–positron pair two beam plasmas have shown an instability, both Weibel and two-stream, depending on beam parameters (Bret *et al.* 2013). Detailed three-dimensional (3D) particle-in-cell (PIC) simulations have been performed for interpenetrating electron–positron shells (Fonseca *et al.* 2003; Silva *et al.* 2003). However, there was no inclusion of a background electron–proton plasma in these models and simulations. Theoretical work using distribution functions and kinetic theory have been performed on relativistic unmagnetised plasmas (Yoon & Davidson 1987; Achterberg & Wiersma 2007; Achterberg, Wiersma & Norman 2007; Yoon 2007) which currently are limited to the simplest cases. Further work is needed in the cold-fluid formalism to explore the instabilities in background electron–proton plasmas with beam electron–proton plasma flows and beam lepton pair plasmas (Bret, Gremillet & Dieckmann 2010).

This paper investigates the Weibel instability in three scenarios: counterstreaming electron beams in background plasma, an electron–positron (lepton) beam in background plasma and an electron–proton (plasma) beam in background plasma where all plasmas are cold. The corresponding dispersion relations are derived theoretically in the cold-fluid formalism and compared with fully relativistic two-dimensional (2D) PIC simulations. The theoretical dispersion relation for the Weibel instability is first reviewed following the work in Pegoraro *et al.* (1996). This dispersion relation is extended to the scenario of three electron populations in which one cold population is at rest with respect to the proton frame at the beginning. It is then further extended to the scenario of a lepton beam incident on a background electron–proton plasma. The lepton beam extension is adapted to the third scenario of a plasma beam incident on a background electron–proton plasma. The relation of the Weibel instability growth rate to the number densities of the plasma species and the beam energies is explored for all cases and compared to PIC simulations. The maximum Weibel instability growth rates are predicted for a range of beam energies and plasma species densities using the newly derived dispersion relations.

2. Theoretical model

2.1. *General dispersion relation*

The generalised dispersion relation of the plasma instabilities in counterpropagating beams in plasma with a general perturbation wavevector is derived in Califano, Pegoraro & Bulanov (1997). The transverse mode of the perturbation represents the Weibel instability. However, it is noted that in highly relativistic beams and asymmetric beams the fastest-growing mode may not be the Weibel instability but the scope of this work is determining the growth rates of transverse magnetic fields, potentially leading to Fermi acceleration. Consequently, the reduced transverse dispersion relation for the Weibel instability for an electron–ion plasma is examined following the work by Pegoraro *et al.* (1996) which is easier to deal with analytically.

An initially uniform plasma contains two counterpropagating electron beams with an immobile neutralising ion background. The electron beams propagate along the x-axis of the system and have initial unperturbed number densities defined as $n_{0\alpha}$ with $\alpha = 1, 2$ denoting the electron species. The ion background has density $n_i = \sum_\alpha n_{0\alpha}$ which neutralises the global electron charge of the system. The global net current density is zero. The initial unperturbed electron beam velocities are defined as $v_{0x\alpha}$ with their three-momenta given by $\boldsymbol{v}_\alpha = c\boldsymbol{p}_\alpha/(m^2c^2 + p_\alpha^2)^{1/2}$. All variables are assumed to depend on y and time. From this, the relativistic dynamics of the electrons are described by the following equations with $\boldsymbol{A}$ the vector potential field defined by the magnetic field $\boldsymbol{B} = \nabla \times \boldsymbol{A}$:

$$p_{x\alpha} - \frac{e}{c}A_x = p_{0x\alpha}, \tag{2.1}$$

$$\frac{\partial p_{y\alpha}}{\partial t} + v_{y\alpha}\frac{\partial p_{y\alpha}}{\partial y} = -e\left(E_y - \frac{v_{x\alpha}}{c}B_z\right), \tag{2.2}$$

$$\frac{\partial n_\alpha}{\partial t} + \frac{\partial(n_\alpha v_{y\alpha})}{\partial y} = 0. \tag{2.3}$$

The electron momenta and densities are coupled with the following Maxwell's equations (Griffiths 2013):

$$\frac{\partial E_y}{\partial y} = 4\pi e\left(n_i - \sum_\alpha n_\alpha\right), \tag{2.4}$$

$$\frac{\partial B_z}{\partial y} = -\frac{4\pi e}{c}\sum_\alpha n_\alpha v_{x\alpha} + \frac{1}{c}\frac{\partial E_x}{\partial t}, \tag{2.5}$$

$$\frac{1}{c}\frac{\partial B_z}{\partial t} = \frac{E_x}{\partial y}, \tag{2.6}$$

$$-\frac{\partial^2}{\partial y^2}E_x = -\frac{1}{c}\frac{\partial}{\partial t}\left(\frac{\partial B_z}{\partial y}\right). \tag{2.7}$$

Maxwell's equations and relativistic dynamics equations are linearised using a plane-wave approximation of the form $\sim \exp(-i\omega t + iky)$ for the velocities, densities and fields with ω being the perturbation angular frequency and k the perturbation wavevector. The applied transverse electric perturbation field is given by $\boldsymbol{E}_1 = E_0\exp(-i\omega t + iky)\hat{\boldsymbol{x}}$. In this linearisation process, the following operations become $\partial/\partial t \to -i\omega$ and $\nabla \to ik\hat{\boldsymbol{y}}$

for ease. It is found that the first-order components for these variables give the following:

$$v_{1y\alpha} = \frac{e}{i\omega m \Gamma_\alpha} \left(E_y + \frac{k}{\omega} v_{0x\alpha} E_x \right), \tag{2.8}$$

$$v_{1x\alpha} = \frac{e}{i\omega m \Gamma_\alpha^3} E_x, \tag{2.9}$$

$$n_{1\alpha} = \frac{e n_{0\alpha} k}{i\omega^2 m \Gamma_\alpha} \left(E_y + \frac{k}{\omega} v_{0x\alpha} E_x \right), \tag{2.10}$$

$$E_y = 4\pi e^2 \frac{\sum_\alpha \dfrac{n_{0\alpha} v_{0x\alpha}}{m\Gamma_\alpha} \dfrac{k}{\omega}}{\left(\omega^2 - 4\pi e^2 \sum \dfrac{n_{0\alpha}}{m\Gamma_\alpha} \right)} E_x. \tag{2.11}$$

When the above definitions of the first-order quantities are introduced into (2.7) with the substitution of (2.5), a sixth-order dispersion relation is found for mode frequency ω and perturbation wavevector k:

$$(\omega^2 - \Omega_a^2)[\omega^4 - \omega^2(k^2 c^2 + \Omega_b^2) - k^2 c^2 \Omega_c^2] - k^2 c^2 \Omega_d^4 = 0, \tag{2.12}$$

where

$$\left.\begin{aligned}
\Omega_a^2 &= \omega_{pe}^2 \sum_\alpha \frac{n_{0\alpha}}{n_i \Gamma_\alpha}, \quad \Omega_b^2 = \omega_{pe}^2 \sum_\alpha \frac{n_{0\alpha}}{n_i \Gamma_\alpha^3}, \\
\Omega_c^2 &= \omega_{pe}^2 \sum_\alpha \frac{n_{0\alpha} v_{0x\alpha}^2}{n_i \Gamma_\alpha c^2}, \quad \Omega_d^2 = \omega_{pe}^2 \sum_\alpha \frac{n_{0\alpha} v_{0x\alpha}}{n_i \Gamma_\alpha c},
\end{aligned}\right\} \tag{2.13}$$

with the non-relativistic plasma frequency $\omega_{pe} \equiv (4\pi e^2 n_i/m)^{1/2}$ and the Lorentz factor $\Gamma_\alpha = (1 - v_{0x\alpha}^2/c^2)^{-1/2}$. The dispersion relation in (2.12) can be solved by a substitution of variables, $u = \omega^2$, reducing the sextic dispersion relation to a cubic equation. This cubic equation can be solved numerically with numpy.roots function in Python. This function involves computing the eigenvalues of the companion matrix (Johnson & Horn 1985).

Three branches can be observed from the solutions to the dispersion relation, two oscillatory modes (Im(ω) = 0) and one exponentially growing mode with a non-vanishing imaginary component (Im(ω) $\neq$ 0). The exponentially growing mode is responsible for the Weibel instability. By defining $\omega = i\gamma$, the growth rate γ can be calculated from the exponentially growing mode as a function of the perturbation wavevector k. Curves for both non-relativistic and relativistic cases of two counterstreaming electron beams with a neutralising ion background are shown in figure 1, showing the growth rate of the Weibel instability as a function of k^2.

The maximum growth rate is achieved in the short-wavelength limit where $k^2 c^2 \gg \Omega_a^2, \Omega_b^2, \Omega_c^2, \Omega_d^2$. When this limit is applied to (2.12), equation (2.14) is returned, which shows no dependence on the wavevector k. In the long-wavelength limit where $k^2 c^2 \sim 0$, the growth rate follows a linear dependence on the perturbation wavevector k given by (2.15). These limits follow from Pegoraro *et al.* (1996). The limits are dependent on the Ω_i^2 terms found in the dispersion relation (2.12), which are determined by the density and
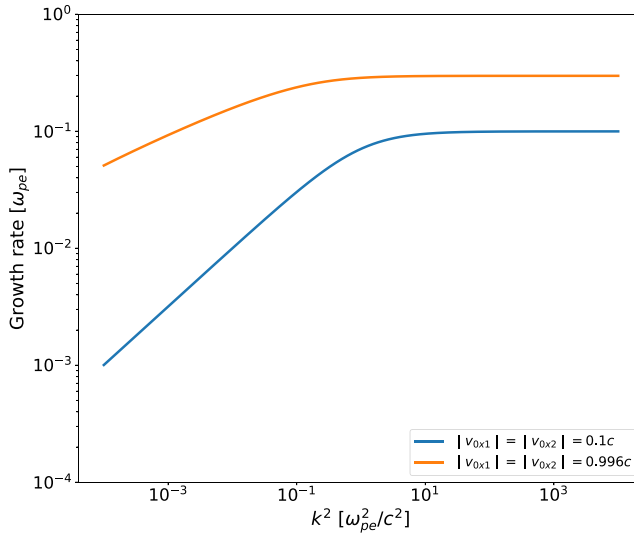
FIGURE 1. Instability growth rate for both a non-relativistic and relativistic case. The two beams have equal number density, i.e. $n_{0,1} = n_{0,2} = n_i/2$. In general, all dispersion relations follow the same pattern where the growth rate reaches a maximum at short perturbation wavelengths.

beam velocity parameters of the system

$$\gamma \approx \{[(\Omega_a^2 + \Omega_c^2)^2 - 4\Omega_d^4]^{1/2} - (\Omega_a^2 - \Omega_c^2)\}^{1/2}/\sqrt{2}, \tag{2.14}$$

$$\gamma \approx kc[(\Omega_a^2\Omega_c^2 - \Omega_d^4)/(\Omega_a^2\Omega_b^2)]^{1/2}. \tag{2.15}$$

The collisional effects between plasma species can be ignored if the electron collision rate is much smaller than the Weibel instability growth rate. The instability growth rate, γ, can be determined in units of the plasma frequency, giving $\gamma = \gamma_g[\omega_{pe}]$, where γ_g is the magnitude of the instability growth rate. Using the formulae for the electron collision rate and the electron plasma frequency from the NRL formulary (Huba 2013), a condition for the collisional effects to be ignored can be determined,

$$\frac{n_e}{T_e^3} \ll \left(\frac{\gamma_g}{\ln \Lambda}\right)^2 9.52 \times 10^{18}, \tag{2.16}$$

where $\ln \Lambda$ is the Coulomb logarithm, n_e is the electron number density in units of cm^{-3} and T_e is the electron temperature in units of eV. For example, if $\ln \Lambda = 10$ and electron density of $n_e = 10^{18} \, \text{cm}^{-3}$ are assumed whereas the instability growth rate is found to be $\gamma = 10^{-1} \, \omega_{pe}$, then the electron temperature must be $T_e \gg 10.2 \, \text{eV}$ for collisional effects to be ignored. Consequently, collisions are neglected in both the derived theoretical models and PIC simulations. If a low-density plasma is considered, then this model assumption is valid.

2.2. *Three-electron-populations case*

Extending from the work in §2.1, the case of three electron populations with an immobile proton background is examined and the dispersion relation determined. This case involves two counterstreaming beams of electrons as previously and an additional third cold electron population with zero drift velocity with respect to the immobile proton
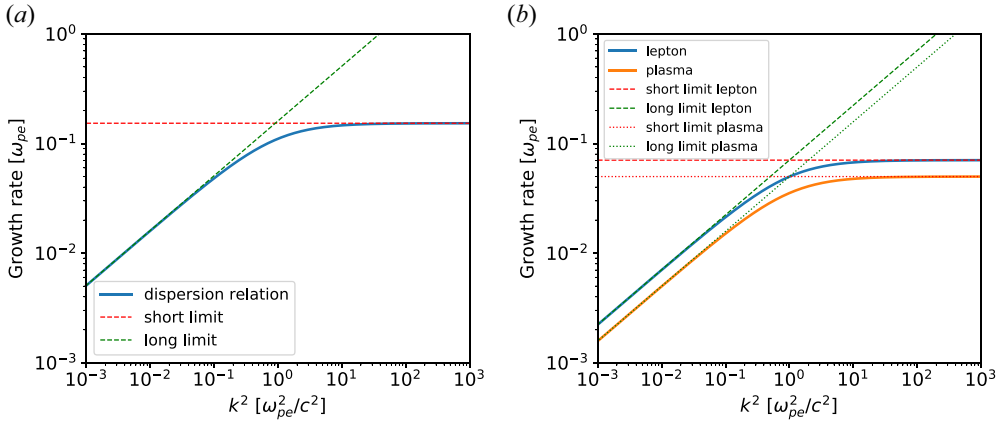
FIGURE 2. Growth rate as a function of the perturbation wavenumber for (*a*) the three-electron-populations case, and (*b*) the lepton-beam case and the plasma-flow case, where the short- and long-wavelength limits are shown by the red and green dashed lines, respectively. The three-electron-populations case has a density ratio of $n_{\text{back}}/2n_{\text{beam}} = 10$ and beam Lorentz factors $\Gamma_\alpha = 3.57$. The lepton-beam and plasma-flow cases have the parameters $n_j/n_p = 0.5$ and $\Gamma_j = 100$. The short-wavelength limit of the lepton-beam case is a factor of $\sqrt{2}$ larger than the same limit in the plasma-flow case.

background. Similarly, the number densities of the three populations must equate the number density of the proton background and net current density in the system is zero. What is found is a dispersion relation with the same functional form as the two-beam case (2.12) with an adjustment to the Ω_a^2 and Ω_b^2 terms

$$
\left.
\begin{aligned}
\Omega_a^2 &= \omega_{\text{pe}}^2 \left[\sum_{\alpha=1,2} \left(\frac{n_{0\alpha}}{n_i \Gamma_\alpha} \right) + \frac{n_{0,3}}{n_i} \right], \\
\Omega_b^2 &= \omega_{\text{pe}}^2 \left[\sum_{\alpha=1,2} \left(\frac{n_{0\alpha}}{n_i \Gamma_\alpha^3} \right) + \frac{n_{0,3}}{n_i} \right].
\end{aligned}
\right\}
\tag{2.17}
$$

The population with $\alpha = 3$ is the cold background electron population and has been shown explicitly for clarity. These terms therefore depend on the number density of the cold electron background. Here Ω_c^2 and Ω_d^2 remain unaffected by the background electron population as the drift velocity is $v_{03x} = 0$ by definition.

The largest difference between the two-beam case and the three-populations case occurs in the relativistic regime. In the two-beam case, Ω_a^2 and Ω_b^2 tend to zero as the Lorentz factors Γ_α increase due to electron inertia. For the three-population case, Ω_a^2 and Ω_b^2 follow $\Omega_a^2 \approx \Omega_b^2 \to \omega_{\text{pe}}^2 (n_{0,3}/n_i)$ in the relativistic limit, which is significant if the stationary density is a large fraction of the total electron density.

The perturbation wavelength limits formulae (2.14)–(2.15) were applied to the three-electron-population case by substituting the new Ω_a^2 and Ω_b^2 terms, this is shown in figure 2(*a*). A large density ratio of $n_{\text{back}}/2n_{\text{beam}} = 10$ is chosen because there is significant change to the original two-electron-beam model used to derive the original limits in Pegoraro *et al.* (1996). Both the short- and long-wavelength limits still agree with the new dispersion relation for the three-electron-populations case.

There are competing modes for the Weibel instability in the three-electron-population case due to beam–beam and beam–background interactions. This is determined by comparing the dispersion relations of the two-beam, one-beam-on-background and the three-population cases. At high background densities of $2n_{\text{back}}/n_{\text{beam}} \geq 1$, the beam–background interaction dominates leading to the three-electron-population case to follow the one-beam-on-background case for all k values. Meanwhile, at low background densities of $2n_{\text{back}}/n_{\text{beam}} < 0.01$, the beam–beam interaction dominates leading to the three-electron-population case following the two-beam case for all k values. In the density regime between those endpoints, the beam–background interaction dominates for $k < 1$ whereas the beam–beam interaction dominates for $k > 1$.

In the cold-fluid formalism, the short-wavelength limit, where $k \to \infty$, gives a saturated maximum instability growth rate (Bret *et al.* 2010). The short-wavelength limit can be analysed analytically to retrieve the scaling with beam velocity and density parameters when working with equal density and speed beams for the three-electron-populations case. For this case, $\Omega_d^2 = 0$ and (2.14) reduces to

$$\frac{\gamma}{\omega_{\text{pe}}} \approx \beta\sqrt{\frac{1}{\Gamma_b(R+1)}}, \tag{2.18}$$

where γ is the maximum growth rate, Γ_b is the beam Lorentz factor, $\beta = v/c$ and $R = n_{\text{back}}/2n_{\text{beam}}$. Equation (2.18) can be applied to the low- and high-beam-density regimes to give

$$\frac{\gamma}{\omega_{\text{pe}}} \approx \begin{cases} \beta\sqrt{\dfrac{1}{R\Gamma_b}}, & \text{for } R \gg 1, \\[2mm] \beta\sqrt{\dfrac{1}{\Gamma_b}}, & \text{for } R \ll 1, \end{cases} \tag{2.19}$$

which are comparable to the scalings found in table I in Bret *et al.* (2010) for electron beams incident on electron–ion plasmas. Consequently, in the three-electron-populations case the maximum growth rate is dependent on the beam-to-background-density ratio and the beam Lorentz factor in the low-beam-density regime. Meanwhile, in the high-beam-density regime the maximum growth rate decouples from the density ratio and is wholly dependent on the beam Lorentz factor.

2.3. *Lepton beam and plasma beam cases*

The lepton beam into a background plasma case is also examined with a similar linearisation process. The electron–positron beam has both net zero charge density and zero current density, i.e. $n_{e^-,0j} = n_{e^+,0j} = n_{0j}/2$ and $v_{e^-,0j} = v_{e^+,0j} = v_{0xj}$ and is travelling in the positive x direction. The background electron–proton plasma has zero net charge ($n_e = n_p$) and zero electron drift velocity with the protons being frozen. There is no restriction between the density of the lepton beam and the density of the background electron–proton plasma as individually they satisfy the neutrality requirements. When the linearisation process is applied to Maxwell's equations and the relativistic dynamics equations, a comparable dispersion relation to (2.12) is found albeit with a change in the

Ω_i^2 terms which are as follows

$$\left.\begin{aligned}
\Omega_a^2 &= \omega_{pe}^2 \left(\frac{n_{0j}}{n_p \Gamma_j} + 1 \right), \quad \Omega_b^2 = \omega_{pe}^2 \left(\frac{n_{0j}}{n_p \Gamma_j^3} + 1 \right), \\
\Omega_c^2 &= \omega_{pe}^2 \frac{n_{0j} v_{0xj}^2}{n_p \Gamma_j c^2}, \quad \Omega_d^2 = \omega_{pe}^2 \frac{n_{0j} v_{0xj}}{n_p \Gamma_j c}.
\end{aligned}\right\} \tag{2.20}$$

The terms are normalised to the background electron–proton plasma frequency, in this case ω_{pe}. Similarly to the three-electron-populations case, the Ω_a^2 and Ω_b^2 terms have a component that is unchanged for differing beam velocities due to the electron density in the background plasma. In the ultrarelativistic limit, $\Omega_a^2 \approx \Omega_b^2 \rightarrow \omega_{pe}^2$, which means the electron inertia becomes wholly dependent on the electron–proton plasma density.

The perturbation wavelength limits formulae (2.14)–(2.15) were applied to the lepton-beam case by substituting the new Ω_i^2 terms, which is shown in figure 2(*b*). A density ratio of $n_j/n_p = 0.5$ is chosen so that the beam density is a significant fraction of the background plasma density, hence the Weibel instability growth rate is appreciable. A beam Lorentz factor of $\Gamma_j = 100$ is chosen such that model is in the relativistic beam regime. There is great agreement between the short- and long-wavelength limits with the dispersion relation for the lepton-beam case.

For a plasma beam incident on a background electron–proton plasma, the derivation of the dispersion relation follows from the lepton-beam case with the change of positrons to protons in the beam. This means the positive charges within the beam are now approximately 1836 times heavier than the electrons although their initial velocities are equal to maintain current density neutrality. The protons in the flow are not frozen. The Ω_i^2 terms derived from the dispersion relation are as follows:

$$\left.\begin{aligned}
\Omega_a^2 &= \omega_e^2 \left(\frac{n_{0j}}{2n_p \Gamma_j} + 1 \right) + \omega_p^2 \frac{n_{0j}}{2n_p \Gamma_j}, \quad \Omega_b^2 = \omega_e^2 \left(\frac{n_{0j}}{2n_p \Gamma_j^3} + 1 \right) + \omega_p^2 \frac{n_{0j}}{2n_p \Gamma_j^3}, \\
\Omega_c^2 &= \frac{n_{0j} v_{0xj}^2}{2n_p \Gamma_j c^2} (\omega_e^2 + \omega_p^2), \quad \Omega_d^2 = \frac{n_{0j} v_{0xj}}{2n_p \Gamma_j c} (\omega_e^2 + \omega_p^2),
\end{aligned}\right\} \tag{2.21}$$

with non-relativistic electron and proton plasma frequencies given by $\omega_e^2 = (4\pi e^2 n_p)/m_e$ and $\omega_p^2 = (4\pi e^2 n_p)/m_p$, respectively. With respect to the lepton beam Ω_i^2 terms, the plasma-flow terms show a factor of 1/2 wherever the density ratio n_{0j}/n_p is found and there is a small addition to all terms due to the perturbation of the protons in the beam ($\omega_e^2/\omega_p^2 \approx 1836$). The overall behaviour of the dispersion is comparable to the lepton-beam case with the difference in the short-wavelength limit growth rate shown in figure 2(*b*). The lepton-beam case shows a factor $\sqrt{2}$ increase in the short-wavelength limit growth rate compared with the plasma beam case in the relativistic or low n_{0j}/n_p density ratio regimes with the same beam Lorentz factors. This is due to the maximum instability growth rate being a function of the density ratio n_{0j}/n_p as seen in table I of Bret *et al.* (2010) in the low-beam-density regime. Therefore, the inherent doubling of the density ratio when comparing the lepton-beam case to the plasma-flow case leads to the $\sqrt{2}$ factor in maximum growth rate.

3. Comparisons with PIC simulations

3.1. *PIC simulations and growth rates*

The PIC simulations are performed using the open-source code Smilei (Derouillat *et al.* 2018). The simulation box is set with $20\lambda_k$ in both the x and y directions where λ_k is the wavelength of the applied electric perturbation field given by $\lambda_k = 2\pi/k$. The perturbation wavevector k is normalised to the reference frequency ω_r/c where in the counterstreaming-beam cases, ω_r is given by the plasma frequency of all electron populations $\omega_{\mathrm{pe}}^2 = 4\pi n_{e,total}e^2/m_e$. In the beam cases, ω_r is given by the background electron plasma frequency $\omega_{\mathrm{pe}}^2 = 4\pi n_p e^2/m_e$. The grid spacing d for both directions is $\lambda_k/8$ for most of the simulations and the timestep is half the grid spacing, $\Delta t = 0.5 * d/c$. The grid spacing $d = \lambda_k/16$ is sometimes used to determine the growth rate at low values of k where the timestep becomes too large to resolve the linear regime. The number of particles per cell for both electrons and protons is 256. The boundary conditions for both fields and particles are periodic. Perturbations are applied via a transverse electric field E_y of sinusoidal form with wavelength λ_k and an amplitude of $0.001\, m_e c\omega_{\mathrm{pe}}/e$ in plasma units. With the parameters defined as such, the timestep and grid spacing are different for each perturbation wavevector k and this is taken into account when the diagnostics are analysed.

The computational Weibel instability growth rates are determined from the electromagnetic energy density diagnostics of the PIC simulations. In CGS units, the electromagnetic energy density is $u = (1/8\pi)(E^2 + B^2)$, using the B_z component for the Weibel instability and the introduction of the plane wave perturbation, the following equation can be found

$$\log(u) = 2\gamma t + \log\left(\frac{B_0}{8\pi}\right), \tag{3.1}$$

where u is the electromagnetic energy density given by B_z, γ is the Weibel instability growth rate, t is time and B_0 is the amplitude of the plane wave perturbation derived from Faraday's law (2.6) on the applied perturbative electric field. The gradient of a linear fit to a log plot of u gives $m = 2\gamma$, which is used to determine the growth rates of the Weibel instability from the PIC simulations at different values of k. These PIC determined growth rates are compared with the growth rates determined from the derived dispersion relations to check the accuracy of the models.

3.2. *PIC simulations for the three-electron-populations case*

In these simulations, the two counterstreaming electron beams are initialised with equal density and magnitude in momentum for the sake of simplicity. In the first set of simulations, the ratio of the counterstreaming beam densities and the background electron population is fixed with $n_{\mathrm{back}}/2n_{\mathrm{beam}} = 0.5$. The Lorentz factor for the counterstreaming beams is varied to see its effect on the Weibel instability growth rate. The comparisons between the linear dispersion theory and PIC code determined growth rates are shown in figure 3 along with the maximum growth rate scaling from (2.18). It should be noted that in the non-relativistic regime, the electrostatic field also grows via an instability. The growth rates for both the transverse Weibel instability and the longitudinal electric field instability were found to be similar thereby the majority electromagnetic energy comes from both the transverse magnetic and longitudinal electrostatic fields.

Focussing on the Weibel instability growth rate, it shows a strong linear dependence with k in the long-wavelength limit, which contrasts with the original two population case in the relativistic regime seen in figure 1. The introduction of the background
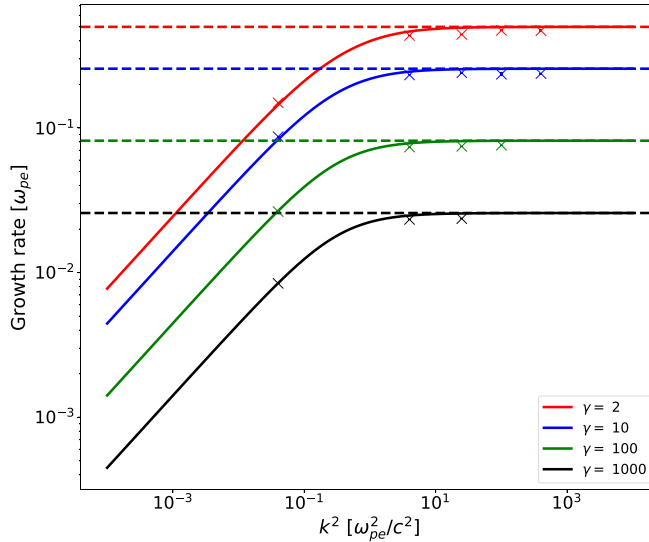
FIGURE 3. Instability growth rates for the three-electron-populations case with differing Lorentz factors. The ratio between the added beam densities and the background density is $n_{\text{back}}/2n_{\text{beam}} = 0.5$. The beam Lorentz factors are determined from the rest frame of the immobile protons and the crosses are the growth rates in the PIC simulations. The dotted lines give the short-wavelength limit from (2.18).

electron plasma with a comparable density to the beams, which affects the Ω_a^2 and Ω_b^2 terms, causes the strong linear dependence to remain in this limit. This is due to competing instabilities for the beam–beam interaction and the beam–background interaction. It is found qualitatively that the beam–beam Weibel instability dominates at high k values and low background plasma densities, whereas the beam–background Weibel instability dominates at low k values and high background plasma densities. For $n_{\text{back}}/2n_{\text{beam}} = 0.5$ found in figure 3, the beam–background interaction dominates, which produces the strong linear dependence for lower values of k. Overall the dispersion relation for this case is slightly overestimating the growth rates determined from the PIC simulations.

The ratio between the counterstreaming beam density and the cold electron background density is changed to see how this would affect the growth rate of the Weibel instability while maintaining the beam Lorentz factor constant. The results from the PIC simulations and comparison with the linear dispersion theory are shown in figure 4 for a non-relativistic and relativistic case. When the background electron population density is small, the functional dependence between the growth rate and k shows similar behaviour in the long-wavelength limit as it approximates the relativistic two-counterstreaming-beams case seen in figure 1. This behaviour vanishes when the density of the background electron population is comparable to the beam densities. Again, the dispersion relation is slightly overestimating the PIC determined growth rates.

An example of the transverse magnetic field B_z progression for the three-electron-populations case is shown in figure 5. At the earlier stages of the PIC simulation, filamentation occurs which causes the bands seen in the first figure. As the magnetic field saturates, the turbulent phase begins causing the filaments to break up. This is more evident in the lepton-beam case.
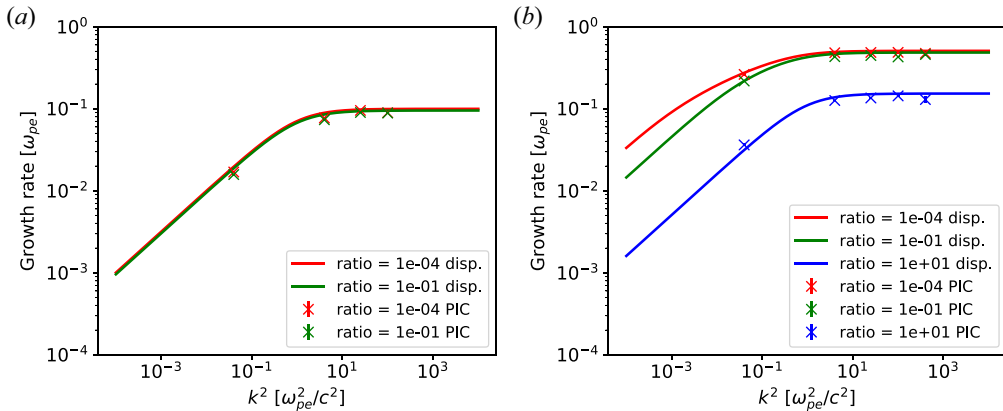
FIGURE 4. Instability growth rates for (*a*) a non-relativistic case of $|v_{0x}| = 0.1c$ and (*b*) a relativistic case of $|v_{0x}| = 0.96c$ with density variations defined by the ratio $n_{\text{back}}/2n_{\text{beam}}$. For the relativistic case, as the density ratio is increased, the growth rate of the instability decreases. In the non-relativistic case, no difference is observed for the density ratios used in the PIC simulations.
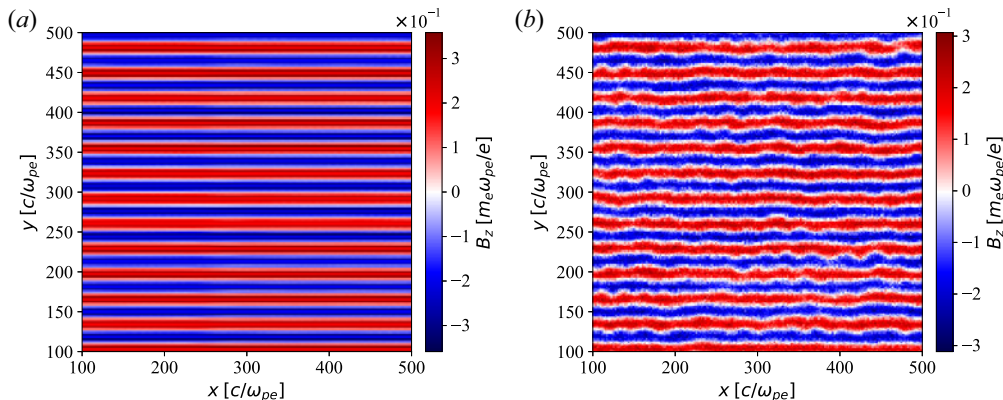
FIGURE 5. Snapshots of B_z magnetic field from PIC simulations for the three-population-case at (*a*) $t = 235.6\,\omega_{\text{pe}}^{-1}$ and (*b*) $t = 4712.4\,\omega_{\text{pe}}^{-1}$. The beam Lorentz factor is $\Gamma = 2$, wavevector $k = 0.2$ and density ratio $n_{\text{back}}/2n_{\text{beam}} = 0.5$. All quantities are in plasma units.

3.3. *PIC simulations for lepton and plasma beams into background electron–proton plasma*

The effect of the Lorentz factor on the Weibel instability growth rate is explored by fixing a beam-to-background density ratio and varying the Lorentz factor. The comparison between the PIC growth rates and the dispersion relations are shown in figure 6(*a*). The functional dependence between the growth rate and k in the long-wavelength limit follows from the non-relativistic two-counterstreaming-beams case even with high beam Lorentz factors. This shows that the behaviour in the relativistic two-counterstreaming-beams case in the long-wavelength limit is unique amongst all the models explored here. The short-wavelength limit shows inverse proportionality to the square root of the beam Lorentz factor as expected from a cold fluid approximation.
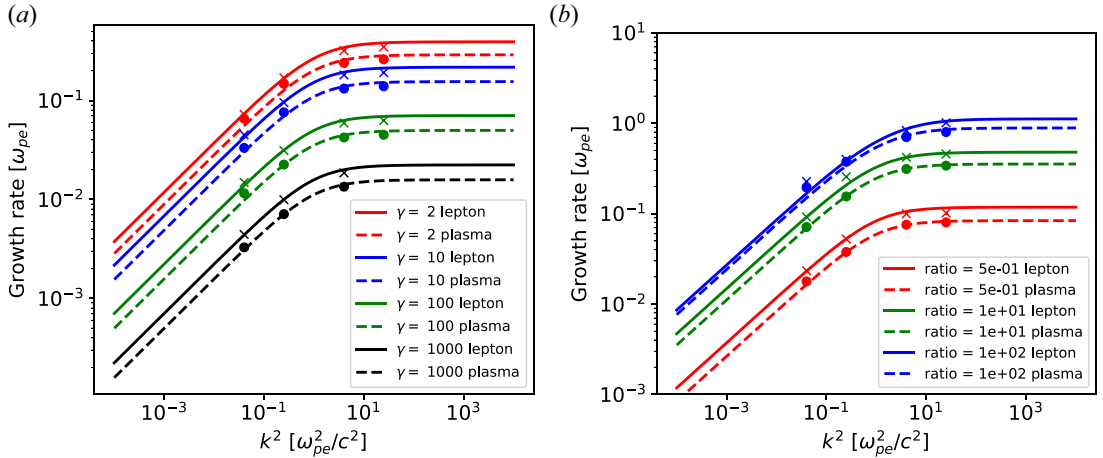
FIGURE 6. Instability growth rates compared with PIC simulations for the lepton-beam case and plasma-flow case. (*a*) Relation between the growth rates and the beam Lorentz factor. The ratio between the beam density and the background density is fixed at $n_j/n_p = 0.5$. The maximum instability growth rate is inversely proportional to $\sqrt{\Gamma_j}$. (*b*) Relation between the growth rates and the density ratio. The beam Lorentz factor is fixed at $\Gamma_j = 35.36$. The crosses show the PIC determined growth rates for the lepton-beam case and the circles represent the PIC determined growth rates for the plasma beam case.

Conversely, the beam Lorentz factor is fixed ($\Gamma_j = 35.36$) and the density ratios are varied for both cases. The growth rates from the PIC simulations and the linear dispersion relation are compared in figure 6(*b*). Regardless of the density ratio between the beam and the background plasma, the growth rate shows the linear dependence in the long-wavelength limit and the maximum growth rate in the short-wavelength limit. Furthermore, the maximum growth rate is proportional to $\sqrt{n_j/n_p}$ The dispersion relation shows good agreement with the PIC determined growth rates.

From the above, the linear dispersion relation is accurate in determining growth rates for a lepton beam inbound on a background electron–proton plasma and a plasma beam on a background electron–proton plasma. Furthermore, the lepton-beam case shows greater Weibel instability growth rates compared with the plasma beam case by a factor of $\sqrt{2}$ in most cases as can be seen in figure 2(*b*). This is explained by the doubling of the beam-to-background-density ratio between the lepton-beam and electron–proton-beam cases seen in (2.20) and (2.21). The numerical methods used to determine the dispersion relation can be extended to predict Weibel instability growth rates.

An example of the transverse magnetic field B_z progression in time for the lepton-beam case is shown in figure 7. At the earlier stages of the PIC simulation, the filamentation occurs and grows exponentially as seen in figure 7(*a*) as with the three-electron-populations case. As the magnetic field saturates, the turbulent phase is shown clearly where islands of magnetic field intensity are found in figure 7(*b*).

3.4. *Discussion about the maximum growth rates*

Now that the numerical method of determining the modes from the dispersion relation of the Weibel instability has been validated by PIC simulations, it can be used to make some predictions on three-electron-populations and lepton-beam systems. It is shown that the growth rate of the Weibel instability reaches the maximum at the short wavelength
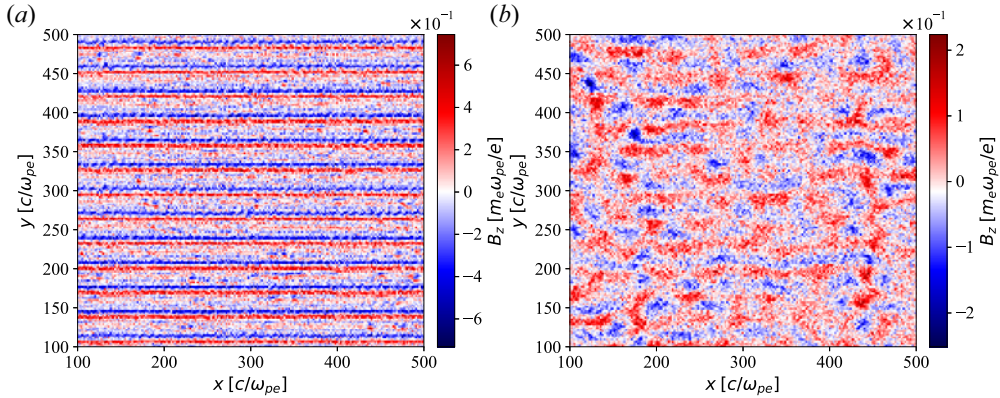
FIGURE 7. Snapshots of B_z magnetic field from PIC simulations for the lepton-beam case at (*a*) $t = 314.16\,\omega_{\mathrm{pe}}^{-1}$ and (*b*) $1413.72\,\omega_{\mathrm{pe}}^{-1}$. The beam Lorentz factor is $\Gamma = 2$, wavevector $k = 0.2$ and density ratio $n_j/n_p = 0.5$. All quantities are in plasma units.
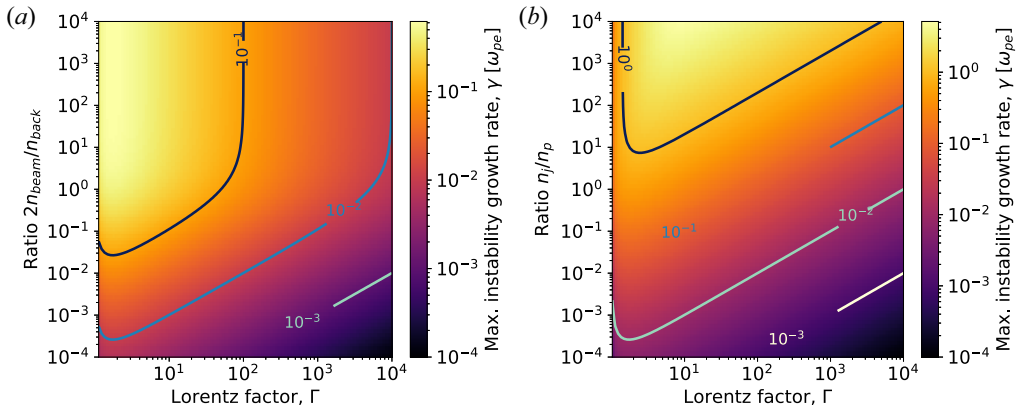
FIGURE 8. Maximum instability growth rate for (*a*) the three-electron-populations case and (*b*) the lepton-beam case for various beam Lorentz factors and beam density ratios. The colour bar shows the maximum achievable growth rate with these parameters. The lepton-beam case growth rates show an overall scale of a factor of 10 greater than the three-electron-populations case.

limit, which is common to all cases of the dispersion relation. Using this fact, an iterative algorithm is used to find the maximum growth rate for a given beam Lorentz factor and density ratio by scanning logarithmically spaced perturbation wavevectors k. A colour map for the three-electron-populations system is shown in figure 8(*a*), where this maximum growth rate is explored. As the counterstreaming beam density increases, the maximum growth rate increases as intuitively expected. However, as the beam Lorentz factor is increased, a non-monotonic behaviour can be seen. The growth rate peaks at $\Gamma \approx 2$ for a high beam density and then decreases as the Lorentz factor is increased.

  A similar analysis is carried out for the lepton-beam case. The maximum growth rate is explored in the beam Lorentz factor and density ratio space and the colourmap is shown in figure 8(*b*). The two cases have comparable outcomes. In general, the lepton-beam case shows higher growth rates in the Weibel instability compared with the three-electron-populations case. The highest growth rate achieved is around beam
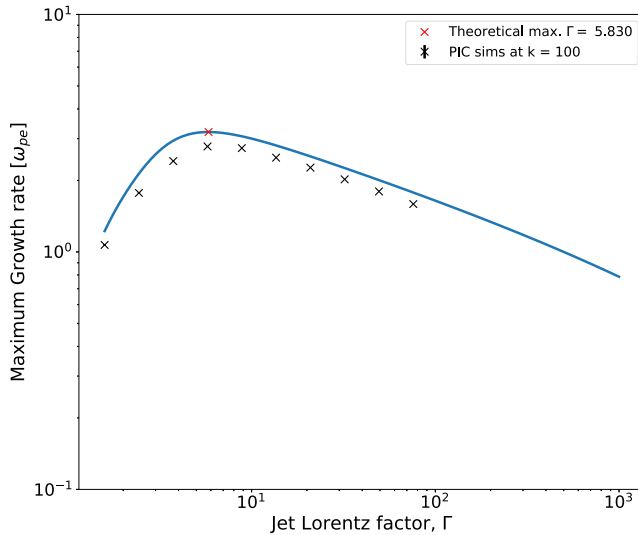
FIGURE 9. Non-monotonic behaviour of the maximum Weibel instability growth rate at a density ratio of $n_j/n_p = 10^3$. The PIC simulations were performed with perturbation wavevector $k = 100$ to ensure the short-wavelength limit is valid. The dispersion relation for the lepton-beam case is slightly overestimating the maximum growth rates compared with those observed in the PIC simulations.

Lorentz factor $\Gamma \approx 10$ with the beam density at 10^4 times higher than the background electron–proton plasma.

The non-monotonic relation between the maximum growth rate and the beam Lorentz factor is explored further. A density ratio of $n_j/n_p = 1 \times 10^3$ is fixed and the beam Lorentz factors scanned with a perturbation wavevector of $k = 100$. This ensures the parameters were in the short-wavelength limit so that the maximum growth rate is returned from PIC simulations (see (2.14) and figure 2). The comparison between the PIC determined growth rates and the theoretical dispersion relation are shown in figure 9. The non-monotonic behaviour is clearly present in the dispersion relation and the PIC simulations, with a systematic overestimation by the dispersion relation. Qualitatively, this shows that the Lorentz factor needs to be optimised for a given beam to background plasma density ratio to achieve the highest growth rate possible. In general, this maximum growth rate is achieved at higher beam Lorentz factors as the beam to background plasma density ratio increases as seen in figure 8(*b*). It should be noted that the plasma-flow case has a comparable relation between the maximum growth rate and the system parameters albeit with a $1/\sqrt{2}$ reduction in maximum growth rate in the relativistic or low-density regimes as explained in § 2.3, which is not shown in this figure.

4. Summary and discussion

A theoretical model has been developed for the Weibel instability in three systems, one with two counterpropagating electron beams in background electron–proton plasma, another with a lepton beam propagating in background electron–proton plasma and the final system for a plasma beam propagating in background electron–proton plasma. The dispersion relations have been derived and found to match PIC simulations with good accuracy. There is a general small systematic overestimation of the Weibel instability

growth rate from the dispersion relations. Moreover, non-monotonic behaviour has been found in both the theoretical dispersion relations and PIC simulations.

The frozen proton/ion background is a useful approximation for determining the linear dispersion relation, but on longer time scales this breaks down and the approximation is no longer true when the instability develops into the nonlinear stage. Coupled with this is the exclusion of any potential ion acceleration mechanisms induced by the possible development of turbulent fields via the Weibel instability. Longitudinal electrostatic fields can compete with the growth of the Weibel instability in certain regimes (Califano *et al.* 1997; Silva *et al.* 2002; Shaisultanov, Lyubarsky & Eichler 2011), but have they largely been ignored in this study as the transverse dispersion equations can still accurately describe the growth rates of the Weibel instability. In the leptonic-beam case, it has been shown that there is a preferential positron acceleration through a quasi-stationary electric field and that ion motion could be included in this effect for longer time scales (Dieckmann *et al.* 2020). Further studies are needed with the inclusion of the free motion of the ion background with a focus on the nonlinear stages while looking at the relation between the beam and background densities. The turbulent properties of the long-time-scale Weibel-induced magnetic fields also need to be explored.

Furthermore, Smilei works in dimensionless units with relative quantities. If collisions are included, then a reference plasma frequency must be set thereby setting a reference plasma density. Hence, the models explored in this paper are valid if a low-density plasma is studied as collisions between plasma species will be negligible in that case as minimum electron temperature will be low, as seen in (2.16). However, the relatively cold background electrons and proton/ions compared with the hot beams will have a strong collisional effect when the reference plasma density is set high. Exploring the interplay of temperature and plasma density on the collisional effect on the models is warranted.

Declaration of interests

The authors report no conflict of interest.

REFERENCES

ACHTERBERG, A. & WIERSMA, J. 2007 The Weibel instability in relativistic plasmas–I. Linear theory. *Astron. Astrophys.* **475** (1), 1–18.

ACHTERBERG, A., WIERSMA, J. & NORMAN, C.A. 2007 The Weibel instability in relativistic plasmas—II. Nonlinear theory and stabilization mechanism. *Astron. Astrophys.* **475** (1), 19–36.

BRET, A., GREMILLET, L. & DIECKMANN, M.E. 2010 Multidimensional electron beam–plasma instabilities in the relativistic regime. *Phys. Plasmas* **17** (12), 120501.

BRET, A., STOCKEM, A., FIUZA, F., RUYER, C., GREMILLET, L., NARAYAN, R. & SILVA, L.O. 2013 Collisionless shock formation, spontaneous electromagnetic fluctuations, and streaming instabilities. *Phys. Plasmas* **20** (4), 042102.

CALIFANO, F., PEGORARO, F. & BULANOV, S.V. 1997 Spatial structure and time evolution of the weibel instability in collisionless inhomogeneous plasmas. *Phys. Rev.* E **56** (1), 963.

CUI, Y.-Q., SHENG, Z.-M., LU, Q.-M., LI, Y.-T. & ZHANG, J. 2015 Two-stage acceleration of interstellar ions driven by high-energy lepton plasma flows. *Sci. China Phys. Mech. Astron.* **58** (10), 105201.

DAWSON, J.M. 1983 Particle simulation of plasmas. *Rev. Mod. Phys.* **55** (2), 403.

DEROUILLAT, J., BECK, A., PÉREZ, F., VINCI, T., CHIARAMELLO, M., GRASSI, A., FLÉ, M., BOUCHARD, G., PLOTNIKOV, I., AUNAI, N., *et al.* 2018 Smilei: a collaborative, open-source, multi-purpose particle-in-cell code for plasma simulation. *Comput. Phys. Commun.* **222**, 351–373.

DIECKMANN, M.E., SPENCER, S.-J., FALK, M. & ROWLANDS, G. 2020 Preferential acceleration of positrons by a filamentation instability between an electron–proton beam and a pair plasma beam. *Phys. Plasmas* **27** (12), 122102.

FERMI, E. 1949 On the origin of the cosmic radiation. *Phys. Rev.* **75** (8), 1169.

FONSECA, R.A., SILVA, L.O., TONGE, J.W., MORI, W.B. & DAWSON, J.M. 2003 Three-dimensional Weibel instability in astrophysical scenarios. *Phys. Plasmas* **10** (5), 1979–1984.

GREGORY, C.D., HOWE, J., LOUPIAS, B., MYERS, S., NOTLEY, M.M., SAKAWA, Y., OYA, A., KODAMA, R., KOENIG, M. & WOOLSEY, N.C. 2008 Astrophysical jet experiments with colliding laser-produced plasmas. *Astrophys. J.* **676** (1), 420.

GRIFFITHS, D.J. 2013 *Introduction to Electrodynamics*. Pearson Education Limited.

HE, M.-Q., DONG, Q.-L., SHENG, Z.-M., WENG, S.-M., CHEN, M., WU, H.-C. & ZHANG, J. 2007 Acceleration dynamics of ions in shocks and solitary waves driven by intense laser pulses. *Phys. Rev.* E **76** (3 Pt 2), 035402.

HIGGINSON, D.P., KORNEEV, P., RUYER, C., RIQUIER, R., MORENO, Q., BÉARD, J., CHEN S.N., GRASSI, A., GRECH, M., GREMILLET, L., *et al.* 2019 Laboratory investigation of particle acceleration and magnetic field compression in collisionless colliding fast plasma flows. *Commun. Phys.* **2** (1), 1–7.

HSU, S.C., MOSER, A.L., MERRITT, E.C., ADAMS, C.S., DUNN, J.P., BROCKINGTON, S., CASE, A., GILMORE, M., LYNN, A.G., MESSER, S.J., *et al.* 2015 Laboratory plasma physics experiments using merging supersonic plasma jets. *J. Plasma Phys.* **81** (2), 345810201. doi: 10.1017/S0022377814001184

HUBA, J.D. 2013 *NRL Plasma Formulary*. Naval Research Laboratory.

JOHNSON, C.R. & HORN, R.A. 1985 *Matrix Analysis*. Cambridge University Press.

LIU, Y.L., KURAMITSU, Y., MORITAKA, T. & CHEN, S.H. 2017 Transition from coherent to incoherent acceleration of nonthermal relativistic electron induced by an intense light pulse. *High Energy Density Phys.* **22**, 46–50.

MAINE, P., STRICKLAND, D., BADO, P., PESSOT, M. & MOUROU, G. 1988 Generation of ultrahigh peak power pulses by chirped pulse amplification. *IEEE J. Quantum Electron.* **24** (2), 398–403.

MONDAL, S., NARAYANAN, V., DING, W.J., LAD, A.D., HAO, B., AHMAD, S., WANG, W.M., SHENG, Z.M., SENGUPTA, S., KAW, P., *et al.* 2012 Direct observation of turbulent magnetic fields in hot, dense laser produced plasmas. *Proc. Natl Acad. Sci. USA* **109** (21), 8011–8015.

PASSONI, M., BERTAGNA, L. & ZANI, A. 2010 Target normal sheath acceleration: theory, comparison with experiments and future perspectives. *New J. Phys.* **12** (4), 045012.

PEGORARO, F., BULANOV, S.V., CALIFANO, F. & LONTANO, M. 1996 Nonlinear development of the Weibel instability and magnetic field generation in collisionless plasmas. *Phys. Scr.* **1996** (T63), 262.

REMINGTON, B.A., ARNETT, D., PAUL, R. & TAKABE, H. 1999 Modeling astrophysical phenomena in the laboratory with intense lasers. *Science* **284** (5419), 1488–1493.

SAGDEEV, R.Z. 1966 Cooperative phenomena and shock waves in collisionless plasmas. *Rev. Plasma Phys.* **4**, 23.

SHAISULTANOV, R., LYUBARSKY, Y. & EICHLER, D. 2011 Stream instabilities in relativistically hot plasma. *Astrophys. J.* **744** (2), 182.

SILVA, L.O., FONSECA, R.A., TONGE, J.W., DAWSON, J.M., MORI, W.B. & MEDVEDEV, M.V. 2003 Interpenetrating plasma shells: near-equipartition magnetic field generation and nonthermal particle acceleration. *Astrophys. J. Lett.* **596** (1), L121.

SILVA, L.O., FONSECA, R.A., TONGE, J.W., MORI, W.B. & DAWSON, J.M. 2002 On the role of the purely transverse Weibel instability in fast ignitor scenarios. *Phys. Plasmas* **9** (6), 2458–2461.

TIDMAN, D.A. 1969 Shock waves in collisionless plasmas. *Plasma Instabilities in Astrophysics, Proceedings of a Conference on Plasma Instabilities in Astrophysics*, 229.

VALENZUELA, J.C., COLLINS IV, G.W., ZICK, T., NARKIS, J., KRASHENINNIKOV, I. & BEG, F.N. 2015 Counter-propagating plasma jet collision and shock formation on a compact current driver. *High Energy Density Phys.* **17**, 140–145.

WEIBEL, E.S. 1959 Spontaneously growing transverse waves in a plasma due to an anisotropic velocity distribution. *Phys. Rev. Lett.* **2** (3), 83.

YOON, P.H. 2007 Relativistic Weibel instability. *Phys. Plasmas* **14** (2), 024504.

YOON, P.H. & DAVIDSON, R.C. 1987 Exact analytical model of the classical Weibel instability in a relativistic anisotropic plasma. *Phys. Rev.* A **35** (6), 2718.